Ferroelectric-controlled magnetoelectric effect at the CrI_3/HfO_2 interface

Tianpeng Duan,[1] Yun Zhang,[2] Jie Jiang,[1] Jingman Pang,[3,*] Min Liao,[1,†] and Qiong Yang[1,‡]
[1]*Hunan Provincial Key Laboratory of Thin Film Materials and Devices, School of Materials Science and Engineering, Xiangtan University, Xiangtan, Hunan 411105, China*
[2]*College of Physicals and Optoelectronic Technology, Collaborative Innovation Center of Rare-Earth Functional Materials and Devices Development, Baoji University of Arts and Sciences, Baoji 721016, China*
[3]*Faculty of Chemistry and Chemical Engineering, Baoji University of Arts and Sciences, 1 Hi-Tech Avenue, Baoji 721016, Shaanxi, People's Republic of China*

(Received 15 December 2023; revised 31 May 2024; accepted 17 July 2024; published 5 August 2024)

The effective manipulation magnetic properties of two-dimensional magnets through electric field presents profound implications for spintronics. In this study, we investigate the ferroelectric-controlled magnetoelectric coupling within the $CrI_3/HfO_2(111)/CrI_3$ heterostructure by using first-principles calculations. It is found that the magnetic moments of CrI_3 are notably responsive to the polarization orientation—either directed towards (P_{in}) or away (P_{out}) from the interface. The polarization of HfO_2 triggers the accumulation (depletion) of screening electrons at the P_{in} (P_{out}) interface, which affects the relative population of the exchange-split spin bands at the interface and thus results in the enhanced (reduced) total magnetic moments of the monolayer CrI_3. The easy magnetization axis of CrI_3 switches from an out-of-plane (P_{out} state) to an in-plane (P_{in} state) direction by the reversal of ferroelectric polarization of HfO_2. Additionally, the Curie temperature (T_C) of monolayer CrI_3 is enhanced by 78% in the P_{out} state. This work provides useful guidelines for the study of interfacial magnetoelectric coupling and design of multiferroic devices.

DOI: 10.1103/PhysRevB.110.054407

I. INTRODUCTION

Multiferroic materials provide numerous opportunities for the advancement of electronic devices, due to the fascinating phenomenon of manipulating one ferroic property through another ferroic conjugate field [1,2]. In particular, utilizing an electric field to control magnetic properties requires less energy in comparison to utilizing a magnetic field or spin-polarized current [3–5], which presents a promising opportunity for the development of next-generation devices with low-dissipation electric writing and fast magnetic reading functions [6–9]. Multiferroic materials can be divided into single-phase multiferroics and layered multiferroics composed of ferroelectric (FE) and ferromagnetic (FM) components. The latter exhibits a higher operational temperature (above room temperature) and superior magnetoelectric coupling due to the pronounced interfacial magnetoelectric effect, which arises from the strain-mediated [10–13] and charge-mediated [14–17] coupling mechanisms. The layered multiferroic materials have been designed with various combinations of ferroelectric candidates such as perovskite-structured $Pb(Fe_{0.5}Nb_{0.5})O_3$, $BaTiO_3$, $Ba_{1-x}Sr_xTiO_3$, $BiFeO_3$, $Pb(Zr_{1-x}Ti_x)O_3$, and $PbTiO_3$ as well as magnetic counterparts such as $La_{1-x}Sr_xMnO_3$, Fe_3O_4, $CoFe_2O_4$, $NiFe_2O_4$, $Ni_{1-x}Zn_xFe_2O_4$, and $Co_{1-x}Zn_xFe_2O_4$ [2,18–20]. However, due to the incompatibility with complementary metal oxide semiconductor (CMOS) technology and the deterioration of ferroelectric behavior at reduced film thickness, the application of layered multiferroic structures is severely restricted at the nanoscale.

Recently, the ferroelectricity has been discovered in the HfO_2 film and its derivatives, for which the ferroelectric behavior originates from the noncentrosymmetric orthorhombic phase of HfO_2 with space group symmetry $Pca2_1$ [21–24]. Owing to the robust ferroelectricity at the nanoscale [25] and great compatibility with the CMOS technology [26], numerous researches have been dedicated to exploring the HfO_2-based nonvolatile memory devices [27–31], which indicates that ferroelectric HfO_2 might be promising to serve as a ferroelectric component in composite multiferroic structures. By using density functional theory (DFT) calculations, a strong charge-mediated magnetoelectric coupling at the Ni/HfO_2 interface driven by FE HfO_2 polarization reversal has been demonstrated in our previous work [32,33], which is verified by subsequent experiments [34]. Vermeulen *et al.* [35] also found that the polarization of the HfO_2 layer has a great effect on the magnetic properties such as magnetocrystalline anisotropy (MAE) and coercive field of the Co layer in Al-doped-HfO_2/Co/Pt heterostructures. However, the presence of dangling bonds at the interface leads to a strong interface interaction between the ferroelectric oxide and magnetic material, which often results in the irreversible modification of the magnetization surface of the magnetic component.

The recent synthesized two-dimensional (2D) magnets, such as CrI_3 [36], $CrGeTe_3$ [37], and Fe_2GeTe_3 [38], offer

*Contact author: pjm_2018@163.com
†Contact author: mliao@xtu.edu.cn
‡Contact author: qyang@xtu.edu.cn

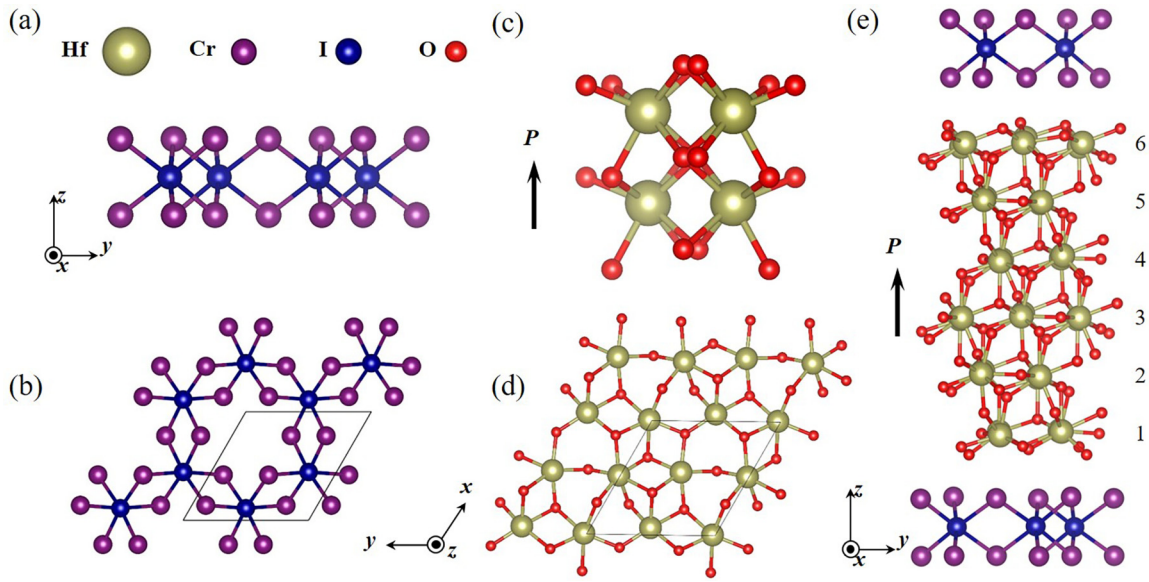

FIG. 1. (a) Side and (b) top views of the monolayer CrI_3. The unit cell is denoted by a solid rhombus. (c) Side view of [001]-oriented $Pca2_1$ HfO_2 unit cell with upward ferroelectric polarization (P). (d) Top view of one Hf-O_2 layer of (111)-oriented $Pca2_1$ HfO_2. (e) Side view of $CrI_3/HfO_2/CrI_3$ vdW heterostructure with upward ferroelectric polarization.

an alternative avenue for exploring multiferroics and magnetoelectric coupling by constructing heterostructures of 2D magnets and ferroelectric materials. Due to the atomically clean interface, such heterostructure can preserve their original magnetic structure and is particularly suitable for the infinite cycle life spintronic devices. For example, Li *et al.* [39] reported that bilayer CrI_3 is switchable between the FM and antiferromagnetic (AFM) phases by reversing the ferroelectric polarization direction of $BiFeO_3$ film, which affects the interaction between the second-nearest neighbor Cr-Cr atoms (interlayer Cr-Cr interaction). Similarly, the interlayer magnetism of bilayer CrI_3 was demonstrated to be switchable between the FM and AFM phases by the control of the ferroelectric polarization direction of α-In_2Se_3 [40]. Moreover, it is found that the polarization reversal of In_2Se_3 can change the orientation of the easy magnetization axis for CrI_3 [41].

In this paper, based on the first-principles density functional theory calculation, we studied the interfacial magnetoelectric effect between the ferromagnetic monolayer CrI_3 (ML CrI_3) and ferroelectric HfO_2 in the constructed $CrI_3/HfO_2(111)/CrI_3$ heterostructure. It is found that the magnetic moments of CrI_3 monolayer are increased (reduced) at the P_{in} (P_{out}) interface. By analyzing the density of states (DOS) of the interface atoms and the charge transfer, it is seen that the accumulation (depletion) of screening electrons at the P_{in} (P_{out}) interface due to the polarization of HfO_2 affects the population of the majority (Cr atom) or minority (I and O) spin DOS, which lead to the charge-mediated interface magnetoelectric coupling. The reversal of ferroelectric polarization can effectively control the switching of the easy magnetization axis of CrI_3 between out-of-plane and in-plane directions, and it can also increase the Curie temperature of CrI_3. Our work will inspire further study to achieving nonvolatile electrical control of atomic-thin van der Waals (vdW) ferromagnets.

II. COMPUTATIONAL DETAILS

Monolayer CrI_3 with the $P\bar{3}1m$ space group [Figs. 1(a) and 1(b)] and ferroelectric HfO_2 layer with the $Pca2_1$ space group [Figs. 1(c) and 1(d)] are chosen as the 2D FM and ferroelectric components, respectively. To minimize the interfacial strong interaction caused by surficial dangling bonds, the (111)-oriented ferroelectric HfO_2, which has the lowest surface energy and is easy to be epitaxially grown on a series of substrates [42–44], is considered in the present work. We constructed $CrI_3/HfO_2/CrI_3$ multiferroic heterostructures by stacking six Hf-O_2 layers (each Hf-O_2 layer includes four Hf and eight O atoms as in our previous studies [45,46]) of HfO_2 and two monolayers of CrI_3 at both surfaces, which allows us to examine the magnetoelectric effect of the CrI_3/HfO_2 interface for polarization pointing into (P_{in}) or away (P_{out}) from the CrI_3 layer using the same structural model with unidirectional polarization of HfO_2, as shown in Fig. 1(e). The in-plane lattice constant of the heterostructure is fixed to the value of ML CrI_3 to avoid the influence of strain to the ML CrI_3 and the central two Hf-O_2 layers are also fixed as the bulk structure to mimic the interior of the HfO_2 film, while the out-of-plane lattice constant and the other internal coordinates are fully relaxed. The thickness of the vacuum gap is at least 20 Å, which is large enough to avoid the possible interaction between the top and bottom surfaces.

DFT calculations are performed in the Vienna *ab initio* simulation package (VASP) with the projector augmented-wave method [47]. The exchange and correlation functional is described by the generalized gradient approximation of the Perdew-Burke-Ernzerhof functional [48]. The plane-wave cutoff energy is set to 450 eV. We adopt the spin-orbital coupling (SOC) for the calculation of magnetic properties. The DFT-D3 approach is used to account for the vdW interactions between layers. The first Brillouin zone is sampled by using a $3 \times 3 \times 1$ Monkhorst-Pack grid for the $CrI_3/HfO_2/CrI_3$

heterostructure. The energy and force convergence criteria are set to 10^{-6} eV and 0.01 eV/Å. Moreover, to describe the strongly correlated 3*d* orbitals of the Cr atom, the effective Hubbard $U_{\rm eff} = 1$ eV is added to the Cr *d* orbitals according to Dudarev's method [49]. The MAE is calculated by using an energy mapping method [50] with the details shown in Sec. III of the Supplemental Material [51]. The Curie temperature (T_C) is calculated based on the Metropolis Monte Carlo (MC) simulations. MC simulation is performed on a 60 × 60 supercell (that contains 7200 Cr ions) with periodic boundary conditions, which is sufficiently large. At each temperature, we used 10^5 MC steps for thermalization and 10^5 MC steps for statistical averaging.

III. RESULTS AND DISCUSSION

As shown in Fig. 1, each ML CrI_3 consists of six I atoms and two Cr atoms, and each Cr is bonded to six neighboring I atoms with Cr located in the center of a hexahedron composed of six I atoms. The optimized lattice constant of freestanding (FS) ML CrI_3 is 7.00 Å without considering the spin-orbit coupling. The magnetic moment of each Cr atom is calculated to be 3.10 μ_B (without considering the effective Hubbard $U_{\rm eff}$), and its band gap is 1.13 eV. The FS ML CrI_3 has an FM ground state with a large perpendicular magnetic anisotropy, which is consistent with the previous studies [52,53]. The optimized lattice parameters *a*, *b*, and *c* of HfO_2 ($Pca2_1$ space group) are 5.25, 5.04, and 5.06 Å, in good agreement with the previous results [32], which lead to the in-plane lattice constants of 7.27 and 7.14 Å, respectively, for the [111]-oriented HfO_2 unit cell. The lattice mismatches between [111]-oriented HfO_2 and ML CrI_3 are less than 3.8%. The calculated band gap of the bulk HfO_2 is 4.39 eV (see Sec. I in the Supplemental Material [51]), which is reasonably consistent with the experimental value (5.60 eV) [54] and previous calculations (4.36 eV) [32]. The atomic configuration of the $CrI_3/HfO_2/CrI_3$ heterostructure is determined by translating the top and bottom CrI_3 layers, respectively, along the interface plane relative to the HfO_2 layer and then fully relaxing the atomic structures to find the heterostructure with global energy minimum (see Sec. II in the Supplemental Material [51]).

We study the magnetization at both CrI_3/HfO_2 interfaces of the heterostructure. The magnetic moments (μ) of the Cr, I, and O atoms at both interfaces are calculated as listed in Table I (with considering the effective Hubbard $U_{\rm eff} = 1$ eV). It is seen that two Cr atoms at the $P_{\rm in}$ interface exhibit a total magnetic moment of 6.653 μ_B, larger than that of the Cr atoms at the $P_{\rm out}$ interface (6.386 μ_B). However, the magnetic moments of I atoms (including $I_{\rm inside}$ and $I_{\rm outside}$) at the $P_{\rm out}$ interface are much larger than those at the $P_{\rm in}$ interface in absolute value. Moreover, the four interfacial O atoms at the $P_{\rm in}$ and $P_{\rm out}$ interfaces also exhibit a total magnetic moment of −0.008 and −0.092 μ_B, respectively. Therefore, the total magnetic moment of the $P_{\rm in}$ ($P_{\rm out}$) interface is increased (decreased) by the ferroelectric polarization relative to that of ML CrI_3, leading to a polarization-induced magnetic moment difference of 0.595 μ_B (1.402×10^{-2} $\mu_B/Å^2$), which is close to that at the $Fe/BaTiO_3$ interfaces ($1.900 \times 10^{-2}\mu_B/Å^2$) [55] and much larger than those at the interface systems with 2D components, such as $CrBr_3$/GaN (0.330×10^{-2} $\mu_B/Å^2$) [56] and $Cr_2Ge_2Te_6/Sc_2CO_2$ interfaces (0.490×10^{-2} $\mu_B/Å^2$) [57]. The interfacial magnetization in the $CrI_3/HfO_2/CrI_3$ heterostructures with the relative position of CrI_3 layers to the HfO_2 layer not at the global energy minimum are also calculated for comparison, and we also calculated the interfacial magnetization when the polarization of HfO_2 reverses (see Tables S2 and S3 in the Supplemental Material [51]). The results show that polarization reversal–induced magnetization variations of other heterostructures are consistent with those in Table I, which indicates that the magnetoelectric effect at the HfO_2/CrI_3 interface is robust and not limited to the most stable interfacial atomic structure. Moreover, the interfacial magnetizations are also calculated by adopting different van der Waals correction methods and SOC (see Tables S4 and S5 in the Supplemental Material [51]), which shows that the ferroelectric-controlled interfacial magnetization variation is independent on the van der Waals correction method and SOC.

TABLE I. The magnetic moments (μ, in μ_B) of two Cr, six I, and four O atoms at both interfaces of the $CrI_3/HfO_2/CrI_3$ vdW heterostructure, respectively, with those of freestanding (FS) ML CrI_3 for comparison. The three I atoms at the interface (surface) side are denoted by $I_{\rm inside}$ ($I_{\rm outside}$). Total magnetic moments in the last row are counted in an interface unit cell, which includes two Cr, six I, and four O atoms at each interface.

Atoms	μ(FS ML CrI_3)	$\mu(P_{\rm out})$	$\mu(P_{\rm in})$
Two Cr	6.422	6.386	6.653
Three $I_{\rm inside}$	−0.296	−0.421	−0.245
Three $I_{\rm outside}$	−0.295	−0.336	−0.268
Four O		−0.092	−0.008
Total	5.831	5.537	6.132

To understand the origin of the polarization-induced magnetization variation at the CrI_3/HfO_2 interface, we further analyze the interfacial electronic structures in terms of the local density of states (LDOS). Figure 2 shows the LDOS projected onto the Cr-*d*, I-*p*, Hf-*d*, and O-*p* electronic states of the interfacial atoms. The overall trend is that the DOS of the interfacial Cr and I atoms at $P_{\rm out}$ ($P_{\rm in}$) interfaces move to the higher (lower) energy relative to that of FS ML CrI_3 due to the polarization-induced potential incline. Since the majority spin DOS of Cr atoms dominates at the Fermi energy, the rightward (leftward) shift of the DOS at the $P_{\rm out}$ ($P_{\rm in}$) interface leads to the depletion (accumulation) of majority spin electrons, resulting in a decrease (increase) of the Cr magnetic moment. On the contrary, because the minority-spin DOS is larger than the majority spin DOS of I atoms at Fermi energy, the polarization-induced DOS shift results in an increase (decrease) of the I magnetic moment at the $P_{\rm out}$ ($P_{\rm in}$) interface. Moreover, it is seen that the DOS of O atoms at the $P_{\rm out}$ interface becomes asymmetric due to the interfacial I $5p$ O $2p$ hybridization [see the DOS in Fig. 2(a)] and, therefore, the rightward shift of the DOS leads to a −0.092 μ_B total magnetic moment of O, which has the same sign with the magnetic moment of I. Because I and O atoms have opposite

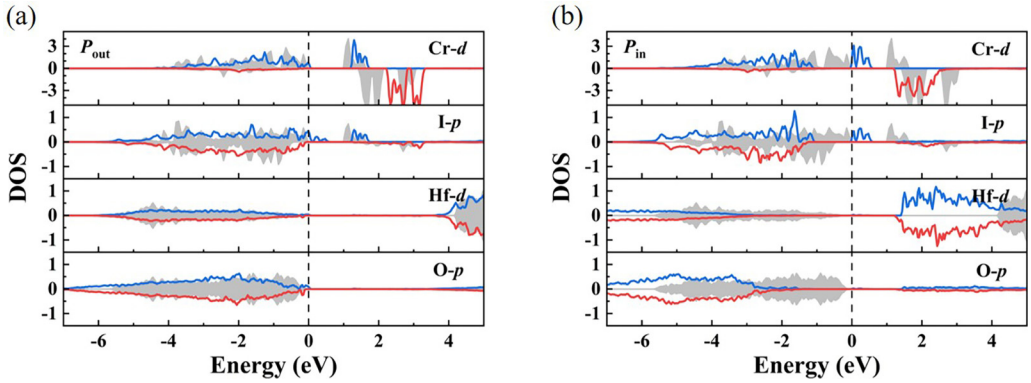

FIG. 2. The DOS projected on each atom at (a) P_{out} and (b) P_{in} interfaces. DOS of Cr, I_{inside}, Hf, and O atoms under the considered energy range are mainly contributed by the Cr $3d$, I $5p$, Hf $5d$, and O $2p$ orbitals, respectively. Each curve represents the average DOS per atom at the interface. The majority- and minority-spin DOS are plotted on the top (positive) and bottom (negative) panels, respectively. The gray filled curves correspond to the DOS of Cr and I atoms in FS ML CrI_3, and Hf and O atoms in bulk HfO_2, respectively. The vertical dashed line indicates the position of Fermi energy (E_F).

direction of the magnetic moment compared with Cr atoms, the total magnetic moment of the interfacial two Cr, six I, and four O atoms decrease (increase) at the P_{out} (P_{in}) interface.

To clarify the polarization-controlled potential distribution and interfacial interaction in the $CrI_3/HfO_2/CrI_3$ heterostructures, the layer-resolved LDOS and interfacial charge transfer are then studied. From the LDOS as shown in Fig. 3(a), it is seen that the potential drops monotonously along the polarization direction, making the Fermi level enter the valence (conduction) band of the CrI_3 layer at the P_{out} (P_{in}) interface, as has been illustrated in Fig. 2. This may cause the charge transfer at the CrI_3/HfO_2 interfaces. To reveal the charge transfer and the induced interfacial interaction, the differential charge densities at the CrI_3/HfO_2 interfaces are calculated as shown in Fig. 3(b) according to $\Delta\rho = \rho_{hetero} - \rho_{HfO_2} - \rho_{CrI_3}$, where ρ_{hetero}, ρ_{HfO_2}, and ρ_{CrI_3} are the charge densities of the heterostructures, HfO_2 layer, and CrI_3 layers, respectively. From Fig. 3(b), we can see that charges are transferred from CrI_3 to HfO_2 at the P_{out} interface and from HfO_2 to CrI_3 at the P_{in} interface, respectively. Based on a Bader analysis [58], CrI_3 layers at P_{out} and P_{in} interfaces are positively and negatively charged by losing and gaining 0.260 and 0.200e, respectively, which is the classical charge screening of the

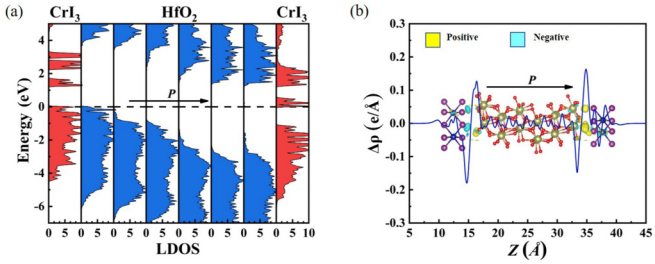

FIG. 3. (a) Layer DOS of the $CrI_3/HfO_2/CrI_3$ heterostructure. Red and blue are for the CrI_3 and HfO_2 layers, respectively. (b) The charge transfer at both interfaces of the heterostructure. The yellow and cyan represent electron gain and loss, respectively. The blue line indicates the planar-averaged differential charge density calculated as $\Delta\rho(z) = \int \rho_{hetero}(x, y, z)dx\,dy - \int \rho_{HfO_2}(x, y, z)dx\,dy - \int \rho_{CrI_3}(x, y, z)dx\,dy$.

ferroelectric polarization. Therefore, the potential incline-induced DOS shift and the corresponding interfacial charge transfer at two interfaces led to a charge-mediated magnetoelectric effect as controlled by the polarization reversal of HfO_2.

The electric field control of magnetic anisotropy and Curie temperature is also important for the application of layered multiferroelectric film. To study the ferroelectric polarization-mediated magnetic anisotropy of the CrI_3 layer at the CrI_3/HfO_2 interface, we adopt the following classical spin Hamiltonian:

$$H = -\frac{J}{2}\sum_{i,i'} \vec{S}_i \cdot \vec{S}_{i'} - \sum_i K\left(S_i^z\right)^2, \tag{1}$$

where S_i is the unit vector of a Cr atom at site i ($S = 3/2$ for CrI_3). The isotropic Heisenberg exchange coupling, denoted by J, spans all first nearest neighbor Cr pairs, while K represents the single ion anisotropy. The values of J and K are obtained by comparing the total energy between the ferromagnetic and antiferromagnetic structures within a single unit cell. The calculated J of the CrI_3/HfO_2 heterostructure with P_{out} and P_{in} states are 4.949 and 4.016 meV, respectively, both larger than that of the FS ML CrI_3 (2.771 meV), due to the interface interaction between the CrI_3 and HfO_2. For the 2D ferromagnetism, it is necessary to study their magnetic anisotropy because it represents a critical parameter to stabilize the long-range magnetic order. To this end, we calculate the total energy for magnetization directions along the [001], [010], and [100] directions with taking into account the spin-orbit coupling. Our results reveal distinct energy differences in the x, y, and z directions of the heterostructure. Specifically, the relative energy differences between the x (y) and z axes are 0.713 (0.548) meV for the P_{out} state and 0.560 (-1.952) meV for the P_{in} state. The previous study [50] demonstrated that the easy magnetization axis of monolayer CrI_3 is perpendicular to the atomic planes, with in-plane [100] and [010] directions equivalent. Thus, our results show a ferroelectric-controlled reorientation of the easy axis in CrI_3 within the heterostructure, which is aligning along the [001] direction for the P_{out} state and the [010] direction for the P_{in} state.

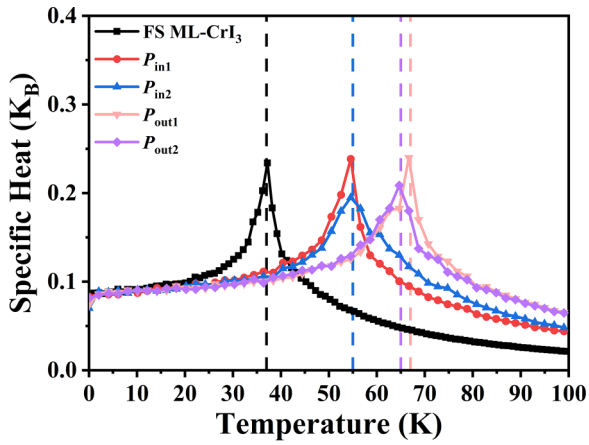

FIG. 4. Calculated specific heat as a function of temperature from Monte Carlo simulations. Black is for the FS ML CrI_3. P_{in1} and P_{out1} (P_{in2} and P_{out2}) represent taking into consideration the magnetic anisotropy energy between the [100] ([010]) and [001] directions for P_{in} and P_{out} interfaces, respectively.

Then, by using MC simulations, we calculate the Curie temperature of the heterostructure and FS ML CrI_3, by looking at the specific heat versus temperature. For simplicity, we estimate the Curie temperature by assuming uniaxial anisotropy. As shown in Fig. 4, the Curie temperature of the FS ML CrI_3 is estimated to be 37 K, which is in accordance with the previous studies [50]. For the heterostructure with the P_{out} states, the Curie temperature is estimated to be 67 K (65 K) by taking into consideration of magnetic anisotropy energy between the [010] ([100]) and [001] directions. For the heterostructure with the P_{in} states, the Curie temperature is estimated to be 55 K, regardless of the specific in-plane directions considered. It is found that the Curie temperatures for the two polarization states of the heterostructure both increase as compared with that of FS ML CrI_3 due to the enhanced exchange interaction J. And the Curie temperature at the P_{out} interface is higher than that at the P_{in} interface, corresponding well to the larger J at the P_{out} interface, which indicates a ferroelectric control of Curie temperature of CrI_3.

IV. CONCLUSIONS

In summary, based on first-principles calculations, we systematically investigated the ferroelectric-controlled magnetoelectric effect of layered multiferroic heterostructure composed of ferroelectric HfO_2 and 2D ferromagnetic CrI_3. It is found that, when the polarization of HfO_2 points away from (into) the CrI_3/HfO_2 interface, the electrons depletion (accumulation) occurs on the CrI_3 to screen the ferroelectric polarization. Since the majority of the spin states of CrI_3 dominate the Fermi level, this ferroelectric polarization–induced electrons depletion (accumulation) leads to a significant decrease (increase) of total magnetic moments of CrI_3, resulting in a charge-mediated interfacial magnetoelectric effect. Intriguingly, it is demonstrated that the easy magnetization axis of CrI_3 is reoriented aligning the [010] and [001] directions, respectively, by the ferroelectric polarization of the HfO_2 layer pointing into and away from the interface. Moreover, the Curie temperature of CrI_3 is notably increased due to the larger exchange interaction when the polarization of the HfO_2 layer points away from the interface, compared to the opposite polarization state. We predict that other HfO_2/2D ferromagnet heterostructures will also exhibit similar magnetoelectric effects as the HfO_2/CrI_3 interface. This work is meaningful for the understanding of magnetic coupling between the attractive HfO_2-based ferroelectrics and 2D ferromagnets and offers a promising scheme for the industrialization of voltage-controlled magnetoelectric memory and logic devices.

The atomic structures were plotted using VESTA software [59].

ACKNOWLEGMENTS

This work was supported by the National Natural Science Foundation of China (Grants No. 12072307, No. 52122205, and No. 12372331), the Outstanding Youth Science Foundation of Hunan Province, China (Grant No. 2021JJ20041), and the Research Foundation of Education Bureau of Hunan Province, China (Grant No. 21A0114). Y.Z. and J.P. acknowledge support from Natural Science Basic Research plan in Shaanxi Province of China (Grant No. 2022JQ-008) and Open Foundation of State Key Laboratory of Surface Physics and Department of Physics (Grant No. KF2022_14).

[1] M. Bibes, Nanoferronics is a winning combination, Nat. Mater. **11**, 354 (2012).
[2] N. A. Spaldin and R. Ramesh, Advances in magnetoelectric multiferroics, Nat. Mater. **18**, 203 (2019).
[3] E. Y. Tsymbal, Spintronics: Electric toggling of magnets, Nat. Mater. **11**, 12 (2012).
[4] S. Manipatruni, D. E. Nikonov, and I. A. Young, Beyond CMOS computing with spin and polarization, Nat. Phys. **14**, 338 (2018).
[5] P. B. Meisenheimer, S. Novakov, N. M. Vu, and J. T. Heron, Perspective: Magnetoelectric switching in thin film multiferroic heterostructures, J. Appl. Phys. **123**, 240901 (2018).
[6] M. M. Vopson, Fundamentals of multiferroic materials and their possible applications, Crit. Rev. Solid State Mater. Sci. **40**, 223 (2015).
[7] M. Fiebig, T. Lottermoser, D. Meier, and M. Trassin, The evolution of multiferroics, Nat. Rev. Mater. **1**, 16046 (2016).
[8] Y. Yin and Q. Li, A review on all-perovskite multiferroic tunnel junctions, J. Mater. **3**, 245 (2017).
[9] T. Hu and E. Kan, Progress and prospects in low-dimensional multiferroic materials, WIREs Comput. Mol. Sci. **9**, e1409 (2019).
[10] T. Taniyama, Electric-field control of magnetism via strain transfer across ferromagnetic/ferroelectric interfaces, J. Phys.: Condens. Matter **27**, 504001 (2015).
[11] X. Li, D. Carka, C. Liang, A. E. Sepulveda, S. M. Keller, P. K. Amiri, G. P. Carman, and C. S. Lynch, Strain-mediated 180° perpendicular magnetization switching of a single domain multiferroic structure, J. Appl. Phys. **118**, 014101 (2015).

[12] A. T. Chen and Y. G. Zhao, Progress of converse magnetoelectric coupling effect in multiferroic heterostructures, Acta Phys. Sin. **67**, 157513 (2018).

[13] F. Motti, G. Vinai, A. Petrov, B. A. Davidson, B. Gobaut, A. Filippetti, G. Rossi, G. Panaccione, and P. Torelli, Strain-induced magnetization control in an oxide multiferroic heterostructure, Phys. Rev. B **97**, 094423 (2018).

[14] Z. Zhou, B. M. Howe, M. Liu, T. Nan, X. Chen, K. Mahalingam, N. X. Sun, and G. J. Brown, Interfacial charge-mediated non-volatile magnetoelectric coupling in $Co_{0.3}Fe_{0.7}/Ba_{0.6}Sr_{0.4}TiO_3$/Nb:$SrTiO_3$ multiferroic heterostructures, Sci. Rep. **5**, 7740 (2015).

[15] R. Gupta, S. Chaudhary, and R. K. Kotnala, Interfacial charge induced magnetoelectric coupling at $BiFeO_3/BaTiO_3$ bilayer interface, ACS Appl. Mater. Interfaces **7**, 8472 (2015).

[16] M. An and S. Dong, Charge-mediated magnetoelectricity: From ferroelectric field effect to charge-ordering ferroelectrics, Acta Phys. Sin. **69**, 217502 (2020).

[17] Y. L. Lu, L. Zhu, Y. Li, N. Wang, F. L. Wang, H. Zheng, Y. G. Wang, and F. M. Pan, Enhancement of charge-mediated magnetoelectric coupling in $Fe_3O_4/SrTiO_3/Ba_{0.6}Sr_{0.4}TiO_3$ heterostructure, J. Phys.: Condens. Matter **32**, 295802 (2020).

[18] D. K. Pradhan, S. Kumari, and P. D. Rack, Magnetoelectric composites: Applications, coupling mechanisms, and future directions, Nanomaterials **10**, 2072 (2020).

[19] J. M. Hu, C. G. Duan, C. W. Nan, and L. Q. Chen, Understanding and designing magnetoelectric heterostructures guided by computation: Progresses, remaining questions, and perspectives, npj Comput. Mater. **3**, 18 (2017).

[20] N. Ortega, A. Kumar, J. F. Scott, and R. S. Katiyar, Multifunctional magnetoelectric materials for device applications, J. Phys.: Condens. Matter **27**, 504002 (2015).

[21] T. S. Böscke, J. Müller, D. Bräuhaus, U. Schröder, and U. Böttger, Ferroelectricity in hafnium oxide thin films, Appl. Phys. Lett. **99**, 10 (2011).

[22] X. Sang, E. D. Grimley, T. Schenk, U. Schroeder, and J. M. Lebeau, On the structural origins of ferroelectricity in HfO_2 thin films, Appl. Phys. Lett. **106**, 16 (2015).

[23] P. Fan, Y. K. Zhang, Q. Yang, J. Jiang, L. M. Jiang, M. Liao, and Y. C. Zhou, Origin of the intrinsic ferroelectricity of HfO_2 from *ab initio* molecular dynamics, J. Phys. Chem. C **123**, 21743 (2019).

[24] W. Ding, Y. Zhang, L. Tao, Q. Yang, and Y. Zhou, The atomic-scale domain wall structure and motion in HfO_2-based ferroelectrics: A first-principle study, Acta Mater. **196**, 556 (2020).

[25] B. Prasad, V. Thakare, A. Kalitsov, Z. Zhang, B. Terris, and R. Ramesh, Large tunnel electroresistance with ultrathin $Hf_{0.5}Zr_{0.5}O_2$ ferroelectric tunnel barriers, Adv. Electron. Mater. **7**, 6 (2021).

[26] S. Beyer *et al.*, FeFET: A versatile CMOS compatible device with game-changing potential, in *Proceedings of the 2020 IEEE International Memory Workshop (IMW)* (IEEE, Piscataway, NJ, 2020), pp. 1–4.

[27] T. Francois, L. Grenouillet, J. Coignus, P. Blaise, C. Carabasse, N. Vaxelaire, T. Magis, and F. Aussenac, Demonstration of BEOL-compatible ferroelectric $Hf_{0.5}Zr_{0.5}O_2$ scaled FeRAM Co-integrated with 130 nm CMOS for embedded NVM applications, in *Proceedings of the IEEE International Electron Devices Meeting (IEDM)* (IEEE, Piscataway, NJ, 2019), pp. 15.7.1–15.7.4.

[28] Q. Yang, L. Tao, Y. Zhang, M. Li, Z. Jiang, E. Y. Tsymbal, and V. Alexandrov, Ferroelectric tunnel junctions enhanced by a polar oxide barrier layer, Nano Lett. **19**, 7385 (2019).

[29] K. Do Kim *et al.*, Transient negative capacitance effect in atomic-layer-deposited $Al_2O_3/Hf_{0.5}Zr_{0.7}O_2$ bilayer thin film, Adv. Funct. Mater. **29**, 1808228 (2019).

[30] D. Lu, S. Crossley, R. Xu, Y. Hikita, and H. Y. Hwang, Freestanding oxide ferroelectric tunnel junction memories transferred onto silicon, Nano Lett. **19**, 3999 (2019).

[31] H. Mulaosmanovic *et al.*, Interplay between switching and retention in HfO_2-based ferroelectric FETs, IEEE Trans. Electron Devices **67**, 3466 (2020).

[32] Q. Yang, L. Tao, Z. Jiang, Y. Zhou, E. Y. Tsymbal, and V. Alexandrov, Magnetoelectric effect at the Ni/HfO_2 interface induced by ferroelectric polarization, Phys. Rev. Appl. **12**, 024044 (2019).

[33] Z. Chen, Q. Yang, L. Tao, and E. Y. Tsymbal, Reversal of the magnetoelectric effect at a ferromagnetic metal/ferroelectric interface induced by metal oxidation, npj Comput. Mater. **7**, 204 (2021).

[34] A. Dmitriyeva *et al.*, Magnetoelectric coupling at the $Ni/Hf_{0.5}Zr_{0.5}O_2$ interface, ACS Nano **15**, 14891 (2021).

[35] B. F. Vermeulen *et al.*, Ferroelectric control of magnetism in ultrathin HfO_2/Co/Pt layers, ACS Appl. Mater. Interfaces **11**, 34385 (2019).

[36] B. Huang *et al.*, Layer-dependent ferromagnetism in a van der Waals crystal down to the monolayer limit, Nature (London) **546**, 270 (2017).

[37] C. Gong *et al.*, Discovery of intrinsic ferromagnetism in two-dimensional van der Waals crystals, Nature (London) **546**, 265 (2017).

[38] Y. Deng *et al.*, Gate-tunable room-temperature ferromagnetism in two-dimensional Fe_3GeTe_2, Nature (London) **563**, 94 (2018).

[39] P. Li, X. S. Zhou, and Z. X. Guo, Intriguing magnetoelectric effect in two-dimensional ferromagnetic/perovskite oxide ferroelectric heterostructure, npj Comput. Mater. **8**, 20 (2022).

[40] H. X. Cheng, J. Zhou, C. Wang, W. Ji, and Y. N. Zhang, Nonvolatile electric field control of magnetism in bilayer CrI_3 on monolayer In_2Se_3, Phys. Rev. B **104**, 064443 (2021).

[41] B. Zhai, R. Cheng, W. Yao, L. Yin, C. Shen, C. Xia, and J. He, Using ferroelectric polarization to regulate and preserve the valley polarization in a $HfN_2/CrI_3/In_2Se_3$ heterotrilayer, Phys. Rev. B **103**, 214114 (2021).

[42] K. Katayama, T. Shimizu, O. Sakata, T. Shiraishi, S. Nakamura, T. Kiguchi, A. Akama, T. J. Konno, H. Uchida, and H. Funakubo, Growth of (111)-oriented epitaxial and textured ferroelectric Y-doped HfO_2 films for downscaled devices, Appl. Phys. Lett. **109**, 112901 (2016).

[43] T. Mimura, K. Katayama, T. Shimizu, H. Uchida, T. Kiguchi, A. Akama, T. J. Konno, O. Sakata, and H. Funakubo, Formation of (111) orientation-controlled ferroelectric orthorhombic HfO_2 thin films from solid phase via annealing, Appl. Phys. Lett. **109**, 052903 (2016).

[44] M. J. Zou, Y. L. Tang, Y. L. Zhu, Y. P. Feng, Y. J. Wang, M. J. Han, N. B. Zhang, J. Y. Ma, B. Wu, and X. L. Ma, Anisotropic

strain: A critical role in domain evolution in (111)-oriented ferroelectric films, Acta Mater. **166**, 503 (2019).

[45] Y. Zhang, Q. Yang, L. Tao, E. Y. Tsymbal, and V. Alexandrov, Effects of strain and film thickness on the stability of the rhombohedral phase of HfO_2, Phys. Rev. Appl. **14**, 014068 (2020).

[46] C. Huang, Y. Zhang, S. Zheng, Q. Yang, and M. Liao, Interface effects induced by a ZrO_2 seed layer on the phase stability and orientation of HfO_2 ferroelectric thin films: A first-principles study, Phys. Rev. Appl. **16**, 044048 (2021).

[47] G. Kresse and D. Joubert, From ultrasoft pseudopotentials to the projector augmented-wave method, Phys. Rev. B. **59**, 1758 (1999).

[48] J. P. Perdew, K. Burke, and M. Ernzerhof, Generalized gradient approximation made simple, Phys. Rev. Lett. **77**, 3865 (1996).

[49] S. Dudarev and G. Botton, Electron-energy-loss spectra and the structural stability of nickel oxide: An LSDA+U study, Phys. Rev. B. **57**, 1505 (1998).

[50] J. L. Lado and J. Fernández-Rossier, On the origin of magnetic anisotropy in two dimensional CrI_3, 2D Mater. **4**, 035002 (2017).

[51] See Supplemental Material at http://link.aps.org/supplemental/10.1103/PhysRevB.110.054407 for electronic structures of monolayer CrI_3 and HfO_2; the atomic structures and magnetic moments at different CrI_3/HfO_2 interface; and the structural model for MAE calculation.

[52] Q. F. Xu, W. Q. Xie, Z. W. Lu, and Y. J. Zhao, Theoretical study of enhanced ferromagnetism and tunable magnetic anisotropy of monolayer CrI_3 by surface adsorption, Phys. Lett. A **384**, 126754 (2020).

[53] Z. Wu, J. Yu, and S. Yuan, Strain-tunable magnetic and electronic properties of monolayer CrI_3, Phys. Chem. Chem. Phys. **21**, 7750 (2019).

[54] V. V. Afanas'ev, A. Stesmans, F. Chen, X. Shi, and S. A. Campbell, Internal photoemission of electrons and holes from (100)Si into HfO_2, Appl. Phys. Lett. **81**, 1053 (2002).

[55] C. G. Duan, S. S. Jaswal, and E. Y. Tsymbal, Predicted magnetoelectric effect in $Fe/BaTiO_3$ multilayers: Ferroelectric control of magnetism, Phys. Rev. Lett. **97**, 047201 (2006).

[56] M. Yang, H. Shu, P. Tang, P. Liang, D. Cao, and X. Chen, Intrinsic polarization-induced enhanced ferromagnetism and self-doped p−n junctions in $CrBr_3$/GaN van der Waals heterostructures, ACS Appl. Mater. Interfaces **13**, 8764 (2021).

[57] W. R. Liu, X. J. Dong, Y. Z. Lv, W. X. Ji, Q. Cao, P. J. Wang, F. Li, and C. W. Zhang, Magnetic anisotropy and ferroelectric-driven magnetic phase transition in monolayer $Cr_2Ge_2Te_6$, Nanoscale **14**, 3632 (2022).

[58] M. Yu and D. R. Trinkle, Accurate and efficient algorithm for Bader charge integration, J. Chem. Phys. **134**, 064111 (2011).

[59] VESTA software, https://jp-minerals.org/vesta/en/.